

AD-A073 848

JAYCOR ALEXANDRIA VA

CONTINUED DEVELOPMENT OF FLUID DYNAMICS MODELS. (U)

APR 79 P J MOFFA, S W CHANG

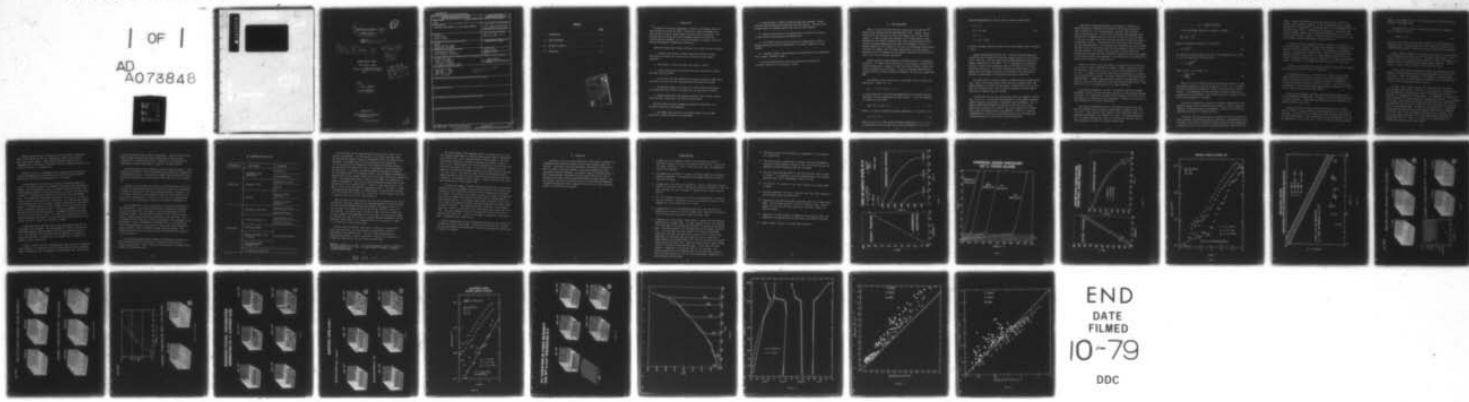
F/G 20/4

N00173-78-C-0421

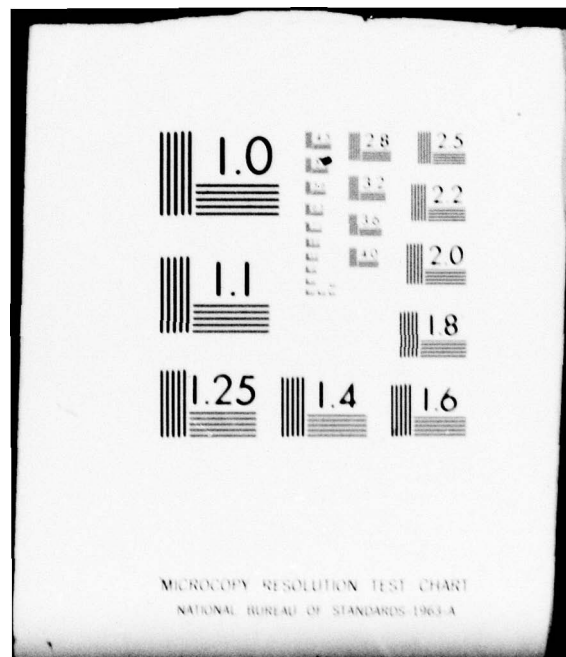
NL

UNCLASSIFIED

| OF |
AD
A073848



END
DATE
FILED
10-79
DDC



ADA073848

⑥
CONTINUED DEVELOPMENT OF FLUID
DYNAMICS MODELS

⑫

APPROVED FOR PUBLIC RELEASE
DISTRIBUTION UNLIMITED

⑨ Final rept.
1 Apr 78-1 Apr 79

⑪ 6 Apr 79

⑫ 36p.

JAYCOR PROJECT #6874

Final Report on NRL

Contract No. N00173-78-C-0421

⑯



⑩
Philip J. Moffa
Simon W. Chang

Submitted to:

Naval Research Laboratories
Washington, D.C.

393453

SP

UNCLASSIFIED

SECURITY CLASSIFICATION OF THIS PAGE (When Data Entered)

REPORT DOCUMENTATION PAGE		READ INSTRUCTIONS BEFORE COMPLETING FORM
1. REPORT NUMBER 6074	2. GOVT ACCESSION NO.	3. RECIPIENT'S CATALOG NUMBER
4. TITLE (and Subtitle) CONTINUED DEVELOPMENT OF FLUID DYNAMICS MODELS		5. TYPE OF REPORT & PERIOD COVERED Final Report 4/1/78-4/1/79
		6. PERFORMING ORG. REPORT NUMBER
7. AUTHOR(s) Philip Moffa Simon W. Chang		8. CONTRACT OR GRANT NUMBER(s) N00173-78-C-0421 <i>new</i>
9. PERFORMING ORGANIZATION NAME AND ADDRESS JAYCOR 205 So. Whiting Street Alexandria, VA 22304		10. PROGRAM ELEMENT, PROJECT, TASK AREA & WORK UNIT NUMBERS
11. CONTROLLING OFFICE NAME AND ADDRESS Plasma Physics Office Naval Research Laboratory		12. REPORT DATE April 6, 1979
14. MONITORING AGENCY NAME & ADDRESS (if different from Controlling Office) DCASMA, San Diego Bldg. 4, AF Plant 19 4297 Pacific Highway San Diego, California 92110		13. NUMBER OF PAGES 32
16. DISTRIBUTION STATEMENT (of this Report) Code 6701 - 1 copy Code 6702 - 1 copy Code 6750 - 1 copy DDC - 12 copies		15. SECURITY CLASS. (of this report) UNCLASSIFIED 15a. DECLASSIFICATION/DOWNGRADING SCHEDULE
17. DISTRIBUTION STATEMENT (of the abstract entered in Block 20, if different from Report)		
18. SUPPLEMENTARY NOTES		
19. KEY WORDS (Continue on reverse side if necessary and identify by block number)		
20. ABSTRACT (Continue on reverse side if necessary and identify by block number)		

CONTENTS

	<u>Page</u>
I. INTRODUCTION.	1
II. CODE DEVELOPMENT.	3
III. SCIENTIFIC RESULTS.	6
IV. CONCLUSION.	13

Accession For	
NTIS GRA&I	<input checked="" type="checkbox"/>
DDC TAB	<input type="checkbox"/>
Unannounced	<input type="checkbox"/>
Justification	<input type="checkbox"/>
By	
Distribution	
Availability Codes	
Dist	Avail and/or special

I. INTRODUCTION

→ A program of continuing development of several fluid dynamic models has been carried out for NRL by JAYCOR. Specifically, major developments and modifications of several large computer codes have been accomplished. This has been done to provide NRL with an expanded capability of modelling diverse physical phenomena, all of which are amenable to analysis utilizing advanced hydrodynamic computational techniques. ←

Among the program modifications performed in this work are the following:

1. Inclusion and testing of thermal conduction routines that have multi-material capabilities and that utilize classical plasma thermal conduction.
2. Multi-material capabilities have been added to FAST2D.
3. A laser energy deposition algorithm has been developed and coupled with both FAST2D and ADINC.
4. A new initializer that generates semi-analytical density, temperature, and velocity profiles has been incorporated into both ADINC and FAST2D.
5. An improved diagnostic that allows for a much better determination of the Rayleigh Taylor instability growth rates has been added to FAST2D.
6. Improved modelling of the planetary boundary layer has been incorporated into both a 2D and NRL's 3D tropical cyclone models.

Utilizing these and other expanded computational capabilities, the following studies have been undertaken:

1. The thermal burn-through of multilayered target foils has been studied for different materials and thicknesses.

2. Rayleigh Taylor instability analyses have been performed. Growth rates have been determined and dispersion relations deduced. The sensitivity of these results to improved spatial resolution has been examined.

3. Dynamic stabilization of the Rayleigh-Taylor instabilities arising in laser fusion has been modelled and demonstrated.

4. The instabilities arising from the use of support webs in pellet designs and those arising from asymmetries in the laser intensity have been studied.

5. Turbulent boundary layer phenomena have been modelled and incorporated into a dynamic atmospheric model.

In the following sections, both these computational advances and scientific results will be discussed in detail.

II. CODE DEVELOPMENT

Both a 1D and a 2D thermal diffusion routine that utilized the $T^{5/2}$ plasma thermal conductivity had been developed at NRL. However, several modifications were necessary for their more general use in laser-fusion studies. In order to study multi-material fusion target designs, space dependence of the thermal conduction coefficient, multiple density arrays, and more convenient temperature units had to be introduced. Also, the thermal conductivity of a mixture of ions had to be calculated (since plastic and glass are commonly used for target construction), and the charge dependence had to be introduced into the thermal coefficient (only the trivial case of D-T with $Z=1$ had been considered).

Another important change needed was the generalization of the boundary conditions. For several test calculations, it was necessary to specify the boundary temperatures. However, for the laser fusion studies, no heat flow across the boundaries was required. In order to implement these different boundary conditions (and any combination thereof), the following changes were made.

The thermal diffusion routines use a tridiagonal solver to update the temperatures. Namely, for 1D,

$$A_i T_{i-1} + B_i T_i + C_i T_{i+1} = D_i \quad , \quad (1)$$

is solved, where the T 's are the new temperatures and the coefficients are functions of the old temperatures and other factors. At the left boundary, for example, we would have:

$$A_1 T_0 + B_1 T_1 + C_1 T_2 = D_1 \quad , \quad (2)$$

where T_0 is some to-be-specified boundary temperature. If we write it as:

$$T_0 = \alpha T_L + \beta T_1 \quad , \quad (3)$$

then we can set it to some specified boundary temperature ($\alpha = 1, \beta = 0$), or assure that there is no heat loss across the boundary ($\alpha = 0, \beta = 1$).

Substituting equation (3) into (2) gives for the new coefficients:

$$A_1 \rightarrow 0$$

$$B_1 \rightarrow B_1 + \beta A_1 \quad (4)$$

$$C_1 \rightarrow C_1$$

$$D_1 \rightarrow D_1 - \alpha T_L A_1 \quad .$$

Of course the same thing can be done for the right boundary with a different α and β .

Another important modification that involved the thermal conduction routines was the introduction of the laser energy directly into the calculations. Previously, the laser deposition had been modelled by driving the boundary temperature of the system. This is inadequate for any detailed analyses of laser fusion experiments since all the details of the laser deposition are missing. By directly inputting the laser energy into the system, both the temporal and spatial distribution of the flux could be modelled, and the amount of energy deposited could be controlled.

We assume that all the laser energy is absorbed through resonant absorption. Hence, the critical density (where the laser frequency equals the plasma frequency) is located and the energy is deposited into the two cells about this critical point. This is done by introducing an energy source term into the thermal diffusion routines.

A routine was written that generated the spatial and temporal distribution of the flux. This was done quite generally so that several different temporal evolutions and spatial illuminations could be employed. Also, a special smoothing algorithm was introduced so that when the critical density point crossed a cell boundary, the finite resolution of the mesh didn't cause any thermal shocks to be generated. Finally, to simulate inhomogeneities in the laser illumination, the ability to introduce controlled perturbations into the laser intensity was added.

Joseph Orens of NRL had developed a semi-analytical technique for generating density, temperature, and velocity profiles that were quasi-static solutions of a set of hydrodynamical equations that modelled a laser-plasma interaction. With his help, subroutines that generated these profiles were introduced into the initializer of both the 1D and 2D codes. In this way, the codes could be initialized with profiles that were known to be essentially correct. The compatibility of these quasi-static solutions and the codes was tested. For a constant laser intensity, only minor changes occurred in the initial profiles when they were stepped in time in the codes for 1000 timesteps. With these initial profiles, we could now do our Rayleigh-Taylor studies with the confidence of knowing that any large changes in the initial profiles that developed in time were due to fluid instabilities which we had initiated in a controlled way.

Finally, in order to study the growth of the Rayleigh-Taylor modes that we initiated, a better diagnostic was needed in FAST2D. Previously, either the location of the ablation layer or a time and space averaged vorticity was used. For example, the ablation layer edge was determined as a function of y and then Fourier analyzed. The Fourier coefficients then determined the mode amplitudes. However, acoustic waves were known to be generated in the ablation layer, and these would shift the ablation edge enough to add a large amount of noise in the determination of the mode amplitudes.

A much better diagnostic was found. The ablation edge was accurately determined for each y and then the mass contained up to the ablation edge was calculated. This summed mass was then Fourier analyzed and found to be much less sensitive to the acoustic wave disturbances. Examples of the quality of this diagnostic will be given in Section III.

Two different parameterizations of the planetary boundary layer have been incorporated into a 2D tropical cyclone model to determine their relative merit. Since the multi-layer scheme is fully vectorized, there is no noticeable computational cost increase in its use. The other parameterization, a matching algorithm was found to be sufficiently accurate, and has been incorporated into NRL's 3D tropical cyclone code.

III. SCIENTIFIC RESULTS

In 1D, the thermal conductivity equation is written:

$$\frac{\partial E}{\partial t} = \frac{\partial}{\partial x} K \frac{\partial T}{\partial x} , \quad (5)$$

where K , the thermal conductivity, is written as:

$$K = K_0 T^{5/2} . \quad (6)$$

For the case of constant density and zero initial temperature, and using $E = 3/2 \rho T$, Equation (5) has the solution:

$$T = T_0 \left(\frac{x+vt}{x_0} \right)^{2/5} , \quad (7)$$

where T_0 and x_0 are constants and

$$v = \frac{4K_0 T_0}{15\rho x_0}^{5/2} . \quad (8)$$

Both the 1D and 2D thermal diffusion routines were tested by driving the boundary temperature according to Equation (7) with $x = 0$. A comparison of the analytical and numerical results for the 1D case are shown in Figure 1. The temperature profiles for several different times are displayed along with the thermal "shock" front position as a function of time. Note that the agreement is excellent.

Also the flux deposition algorithm was checked by depositing a fixed amount of energy into the system and then diffusing it with the boundary condition of zero flux across the boundaries. Conservation of energy was observed to one tenth of a percent accuracy.

In order to test the multi-material capabilities of the 1D thermal conduction routine, the following study was undertaken. We reproduced the test of Figure 1 for a pure D-T (deuterium-tritium) plasma and then repeated the calculations with a 1μ thick foil of different materials inserted into the

system. "Shock" front position versus time plots similar to the one in Figure 1 are displayed in Figure 2. As can be seen, glass (S_2O_2), copper, and gold foils of the densities stated were used. All of these materials slow down the thermal "shock". Since gold has the highest Z , ionization, and since the thermal conductivity is inversely proportional to Z , it inhibits the flow most strongly. However, at large distances from the foils, all the results seem to display approximately the same velocity.

In order to study the asymptotic region of Figure 2, a new series of runs was performed. The pure D-T results were compared to runs where one and two micron slabs of glass were inserted. This comparison is presented in Figure 3. As expected, the thermal "shock" front is slowed down more when passing through the thicker slab. At large distances from the slab, the velocity of the no-slab case should be recovered. This seems to be the case. However, differences in the temperature profiles persist for long times.

In order to study ablation layer Rayleigh-Taylor instabilities, numerical experiments were performed using the code FAST2D.

As mentioned previously, we initialized the system using the steady state, semi-analytical solutions of Orens for our starting temperature, density, and pressure profiles. A dispersion relation is obtained by initially perturbing the density profile at its peak. The first ten modes are excited with equal amplitudes and random phases corresponding to a total initial density perturbation of eight percent.

Using the new diagnostic described previously, the amplitudes of the first three modes were determined. An example of a plot of these amplitudes is given in Figure 4. Growth rates were determined from the exponentially growing regions of such curves.

Figure 5 shows the dispersion relation obtained from four different runs as labelled. The first three runs were performed with a 60 cell by 20 cell mesh. For these runs, a 1μ resolution in the x-direction was used for the non-stretched cells. The y-resolution for the three runs were 1, 2, and 4μ respectively. For the last run, a 120 cell by 20 cell mesh was employed.

Hence, Δ_x was reduced to 0.5μ . This increased resolution produced minimal changes in the growth rates.

The shaded area in Figure 5 corresponds to the classical Rayleigh-Taylor dispersion relation,

$$\gamma = \sqrt{kg}; k = 2\pi/\lambda. \quad (9)$$

The width of the region is due to the variability of g , the acceleration. Although we have a constant laser flux of 10^{13} watts/cm², the mass of the system decreases because of outflow and, hence, the acceleration increases.

Another important aspect of our research on the ablation layer Rayleigh-Taylor instability involves a study of its dynamic stabilization. Boris proposed that by oscillating the laser intensity at some given frequency, the growth of some of the Rayleigh-Taylor modes could be inhibited. The frequency is picked in order to damp the most destructive modes.

Our most recent dynamic stabilization studies using FAST2D are shown in Figure 6. Note that these calculations were performed on an older version of the code. Hence, the temperature of the boundary is specified rather than the laser flux, and the diagnostic for determining the mode amplitudes is not as clear as the example shown in Figure 4.

The upper row of figures displays the time evolution of the density with no dynamic stabilization. Note that by 7nsec the shell is eaten through. For the dynamically stabilized case, shown in the bottom row, the shell maintains its integrity past the 9nsec point. The temperature was oscillated with a frequency of 1.25 cycles/nsec and an amplitude of 125 eV. It is displayed in the lower left hand corner along with the target velocity. Note that for the stabilized case (solid line) almost twice the target velocity is achieved prior to shell break-through. In the upper right hand corner, a comparison of the mode amplitudes with and without dynamic stabilization is presented. The crosses refer to the first mode in the stabilized case, whereas, the circles and squares represent the first and second modes respectively for the non-stabilized run. Again, it is clear that the stabilization has inhibited the Rayleigh-Taylor growth rates.

Another potential cause of instabilities on the surface of the target shell arises from the use of thin membranes to support inner shells in multi-shell fusion targets. These support membranes (webs) can cause inhomogeneities in the density distribution. We have studied the instabilities arising from these in a schematic way.

FAST2D was used in a slab geometry mode. Besides our initial density profile, the membrane was represented by an osculating, Gaussian density perturbation consisting of the same material as the target.

A uniform amount of mass for each y-row was distributed between two x-cells. The center of mass of the membrane lied along a prescribed Gaussian. Because of grid stretching for large x, and finite resolution effects, this uniform membrane appears as the irregular shape in the upper left hand corner of Figure 7. The density was chosen to be 0.125 g/cc in the unstretched cells. For comparison, the maximum slab density is 0.315 g/cc. The rest of Figure 7 gives the time evolution of the density. One sees that the presence of the membrane gives rise to a large "T-shaped" perturbation in the ablation region. A detailed study of the early timesteps shows that this mass flow arises from thermal conduction effects. Initially, the membrane is colder and denser than the surrounding plasma. The membrane heats and loses mass, but the heating is much more rapid. This leads to a pressure profile that forces mass towards the center in the y-direction and out away from the slab in the x-direction. Hence, the "T-shape" is formed.

Further tests were performed using a less dense membrane and one displaced away from the target. The upper sequence of Figure 8 shows how the disturbance develops when the membrane density was reduced by a factor of five. The lower half is for the case when the membrane is displaced 5μ away from the target. For both cases, the characteristic "T-shape" still develops, albeit, more slowly.

Figure 9 contains the first three mode amplitudes for the first membrane test discussed. For comparison, the first mode amplitude from our standard density perturbation run is represented by the straight line. One sees that

for the two cases the growth rates are comparable. These calculations have given a strong indication that these support webs can lead to large instabilities in the ablation process. Further work, both numerical and experimental, should be undertaken to study this in greater detail.

All high intensity lasers produce non-uniform intensity patterns. These intensity variations will cause non-uniform heating leading to inhomogeneities in the ablation process. The question of whether these variations in laser energy are transmitted to the inner edge of the target shell is an important one.

In order to try to answer this question, we performed some calculations in which a 5% sinusoidal perturbation of the laser intensity was introduced. In Figure 10, the case for a 200μ wavelength disturbance is presented. As can be seen, the ablation rate variation follows the laser intensity variation and the target buckles. At least for this case, the transverse heat conduction is not large enough to smooth out the thermal inhomogeneities.

We also undertook a study of the effects of varying the wavelength of the perturbation. It was found that much shorter wavelength disturbances did not appreciably affect the target. This can be understood from the following argument. The sinusoidal disturbance in the y-direction should lead to a damped thermal disturbance traveling in the x-direction. This disturbance should e-fold over a distance comparable to the wavelength of the perturbation. Hence, disturbances of wavelength 10μ will not appreciably affect the target which is on the order of $10-40\mu$ away from the absorption region, whereas the 200μ disturbance strongly warps the target. These results should be of use in the design of the high powered lasers necessary in fusion research.

Two different parameterization schemes of the planetary boundary layer (PBL) have been tested and proposed for incorporation into the NRL 3D tropical cyclone model. Table 1 shows all the different PBL parameterization schemes that have been tested.

PBL PARAMETERIZATION TESTED

CONFIGURATION	BASIC MODELS	VARIATIONS
Single-Layer	Aerodynamic Drag Coefficient	Constant C_D
		Wind Dependent C_D
	Deardorff (1972)	Constant PBL Height
		$\frac{\partial h}{\partial t} \neq 0$
	Matching	Arya's Universal Functions
		Yamada's Universal Functions
	Constant K Coefficient	Unconditional Mixing
		Conditional Mixing
	O'Brien's Parabolic K	Unconditional Mixing
		Conditional Mixing
Multi-Layer	Busch <u>et al</u> Model	
	Meller and Yamada's Level II Closure	Various Mixing Lengths
	Two-Parameter Model (Marchuk, 1977)	
	Ri Adjustment (Chang 1979)	

The first type is to be used when there will be several layers in the tropical cyclone model. For this purpose, an efficient, multilayer model for resolving the thermal, moisture, and momentum fields in the PBL has been developed. The surface heat flux can be generated by two mechanisms: (1) the convective mixing depending on the temperature difference between the surface and the screen level; and (2) the mechanical mixing depending on the wind stress. In the PBL, the heat and momentum exchanges are computed by a Richardson number (Ri) adjustment scheme. Heat and momentum exchanges are computed mainly due to thermal instability arising under convectively unstable conditions. The computational scheme is based on the concepts of conservation of enthalpy and momentum. Case studies show good agreement between model results and the Great Plains Experiment data.¹ Figure 11 shows the evolution of the PBL as illustrated by the potential temperature profile. The model is capable of reproducing the PBL heights, the overshooting, the sharpening of the inversion, the slightly stable lapse rate in upper PBL, and the unstable lapse rate in lower PBL that are evident in the observation.

Since no detailed PBL observations have ever been attempted during tropical cyclones over the ocean, comparison has been made between this efficient model and the more sophisticated and much more expensive PBL model of Busch et al. The two models are integrated from the same initial condition typical of a hurricane PBL. The results shown in Figure 12 after 12 hours of integration of the two models agree remarkably well in PBL depth, the strength and height of the inversion, the radial velocity, the mean potential temperature, and the mean water vapor content. The computational cost of the Busch et al model is 12 times that of the efficient model.

Since no explicit diffusion coefficient is involved in this efficient model, the time step is not restricted by the computational stability requirement of the diffusion term. The five minute time step used in obtaining these results is what is currently allowed by the split-explicit integration scheme used in the NRL tropical cyclone model.

¹Reported in Chang, S. W., 1979: "An Efficient Parameterization of Convective and Non-Convective PBL for Use in a Dynamic Model", to appear in Journal of Applied Meteorology.

The second boundary layer parameterization is designed for use in the NRL tropical cyclone model in which the whole boundary layer is represented by one model layer. Here, the generalized similarity theory is utilized. The "matching technique" discussed by Blackadar and Tennekes is used to obtain a set of PBL equations that has the characteristics of both the mixed layer and the constant flux layer. By scaling this matched set of PBL equations, non-dimensional gradient equations containing universal functions A, B, and C result. By using the proper scales and observational data, Yamada computed the values of these universal functions that show the least scattering. The polynomial form of Yamada's universal functions also facilitates vectorization of the computer code.

To further test Yamada's functions under extreme conditions, the matched equations are used to diagnose the surface fluxes based on the interior flow characteristics of twenty-four different 12 hour integrations of the Busch et al model. The conditions under which the Busch et al model are integrated are highly non-steady with stabilities varying from the strongly stable to the strongly unstable. The diagnosis using Yamada's functions yields a high bias in both the unstable and stable cases when evaluating the surface stress as shown by Figure 13. The diagnosis produces a high bias in the unstable cases and a low bias in the stable cases in evaluating the surface water vapor flux. Very good agreement is found in surface water vapor flux for nearly neutral cases (Figure 14). These biases, however, decrease with time when the PBL is approaching quasi-steady state.

The PBL parameterization using the matching technique has been tested with a 2D and 3D tropical cyclone model. Preliminary results show that cyclones with very good dynamic and thermodynamic structure are generated and maintained at realistic intensity.

IV. CONCLUSION

In sections II and III, we described many of the specific computational advancements and scientific studies that have been completed under this contract. Since many of the codes mentioned, and especially subsections of them, are used in other NRL projects, these accomplishments have other uses that we have not described. For example, some of the modifications in the 1D code have been incorporated into the code FLAME which is used in reactive flow studies involving complicated chemical energy release. Also, the 2D tests involving varying grid resolution and the improved diagnostic for determining ablation layer irregularities are of use in the calibration studies of turbulence closure models.

FIGURE CAPTIONS

1. A comparison of the numerical results of DIFFUL (points) with the analytical solutions (lines) for the thermal diffusion test. On the left, the "shock" position vs. time is shown and on the right, the temperature profiles are displayed.
2. The thermal burn through of 1μ slabs of different materials as labeled is modeled using DIFFUL. The decrease of the thermal conductivity through the slabs is evident.
3. A comparison of thin shell burn through for 1 and 2μ slabs and a no-slab control run for longer times. Although the velocities converge at longer distance from the slab, the differences in temperature and "shock" position persist.
4. The first three mode amplitudes for one of the Rayleigh-Taylor simulation runs are displayed. The growth rates can be determined accurately in the exponentially rising region (here $\sim 3-5$ nsec).
5. A comparison of all of the determined growth rates with the classical Rayleigh-Taylor dispersion relation (shaded area). Note that the improved resolution does not significantly change the growth rates.
6. A demonstration of the dynamic stabilization of some of the most damaging Rayleigh-Taylor unstable modes. The upper sequence shows a time evolution of the slab when an initial density perturbation is applied at the density peak. The lower sequence is for the same case but with dynamic stabilization. As can be seen, the shell maintains its integrity longer when stabilized. The lower left hand corner contains a plot of the driving temperature for the stabilized case (upper half) and a comparison of target velocity for the stabilized (solid line) and non-stabilized (dashed line) calculations (lower half). Note that almost twice as large a target velocity is achieved in the stabilized case. In the upper right hand corner is a comparison of the growth rates for the two cases. The crosses represent the first mode amplitude for the stabilized case and the circles and squares show the first and second modes, respectively, for the non-stabilized calculation.

7. The time evolution of the ablation of a target shell in the presence of a support web.
8. The same as Figure 7 except that in the upper sequence the membrane's density has been reduced by a factor of five, and in the lower one the membrane has been displaced 5μ away from the target.
9. The first three mode amplitudes for the web calculation that was shown in Figure 7. For comparison, the first mode amplitude of the standard Rayleigh-Taylor test is represented by the solid line.
10. The effect of a 5% variation in the laser intensity on a plasma target is shown.
11. Potential temperature profiles at different local mean times computed by the Richardson number adjustment model.
12. Comparison of the Richardson number adjustment model with the Busch et al model. Results shown are after 12 hours of simulation time. The two models are initialized with the same initial conditions typical of a tropical cyclone.
13. Comparison of surface stresses as computed by the Busch et al model and diagnosed by the generalized similarity theory with Yamada's functions.
14. Same as figure 13 except for surface water vapor flux.

TEST OF DIFFU1 (PURE D-T)

$$T = T_0 \left\{ \frac{r + Vt}{r_0} \right\}^{2/5}$$

$$V = \frac{4K_0 T_0^{5/2}}{15\varrho r_0}$$

$$T_0 = 50 \text{ eV}$$

$$= 8.96 \mu/\text{nsec}$$

$$r_0 = 0.1\mu$$

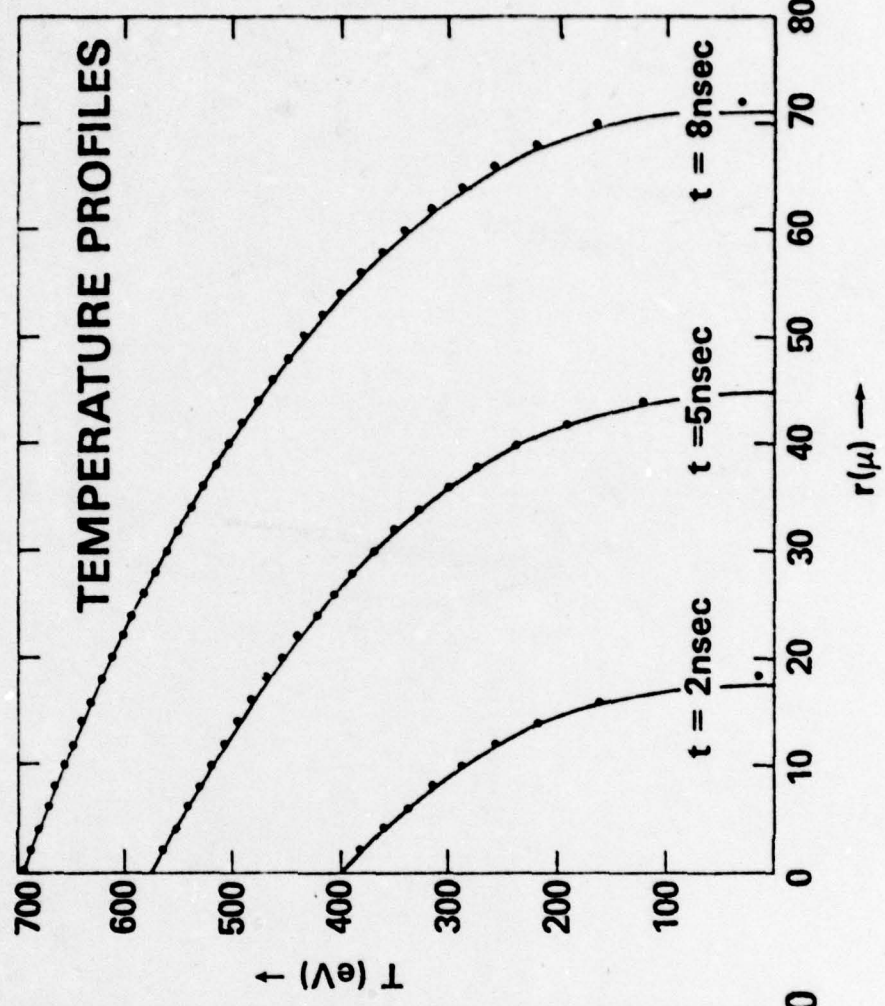
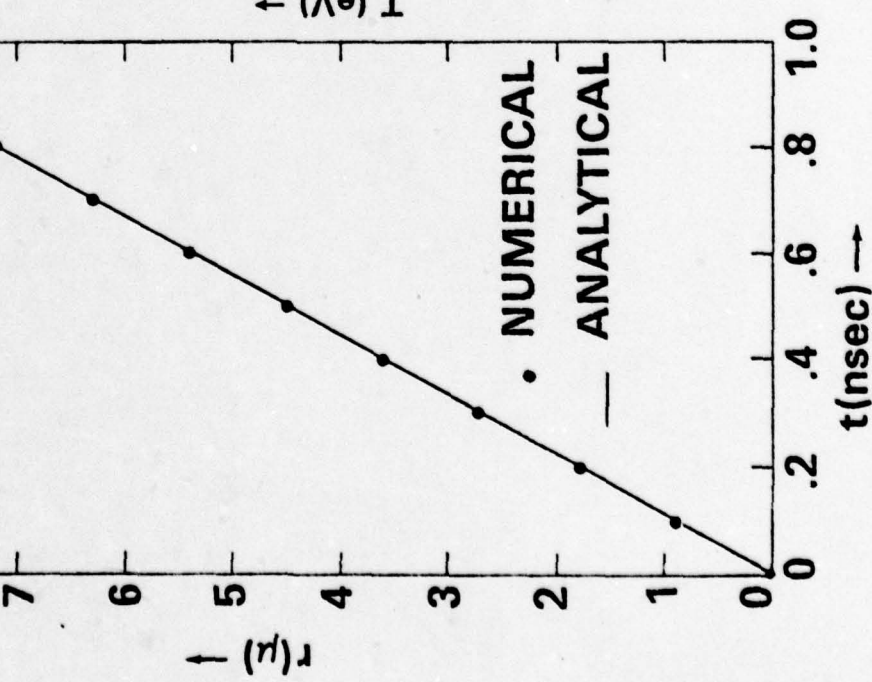


Figure 1

THERMAL BURN THROUGH OF 1μ THICK SLABS

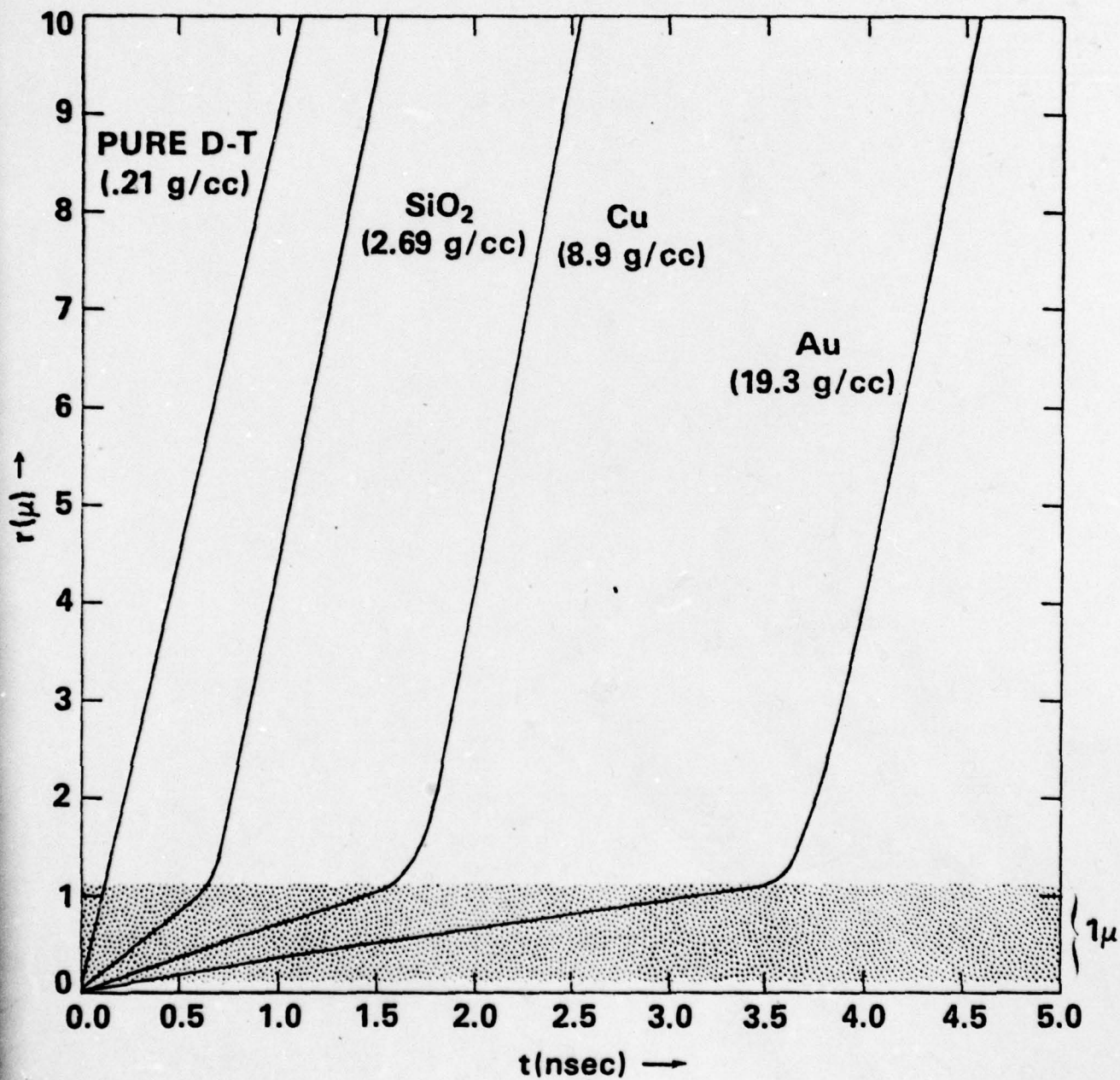


Figure 2

ASYMPTOTIC RESULTS FOR
THIN SHELL BURN THROUGH

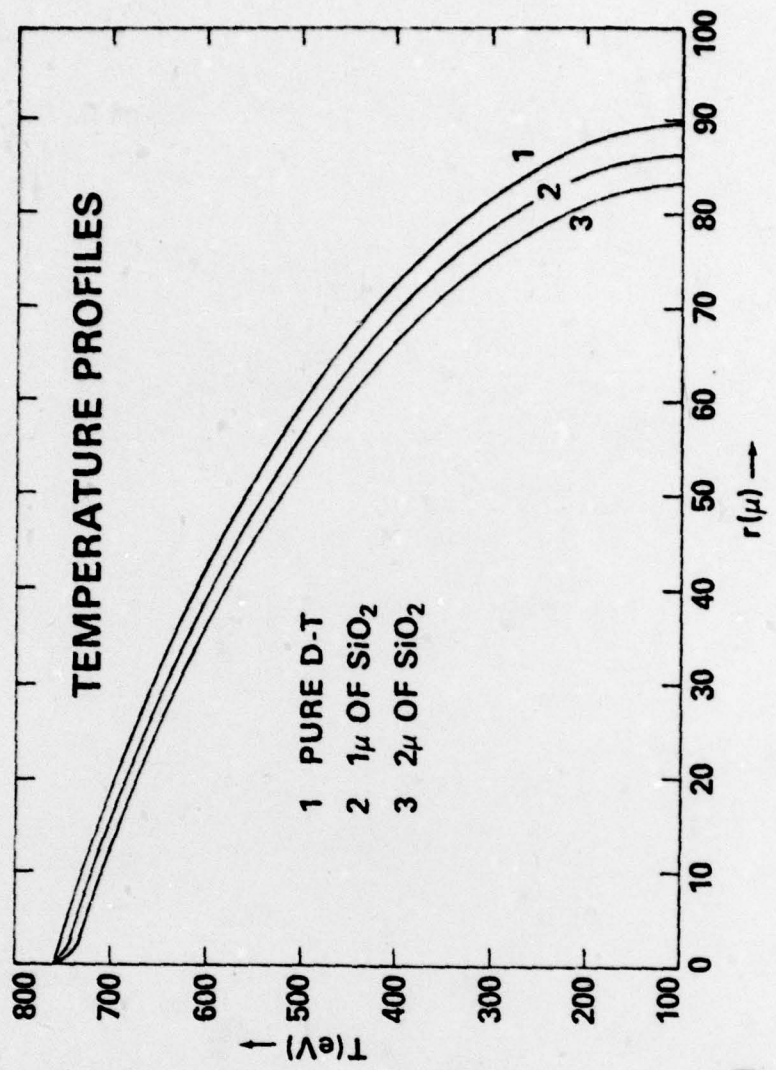
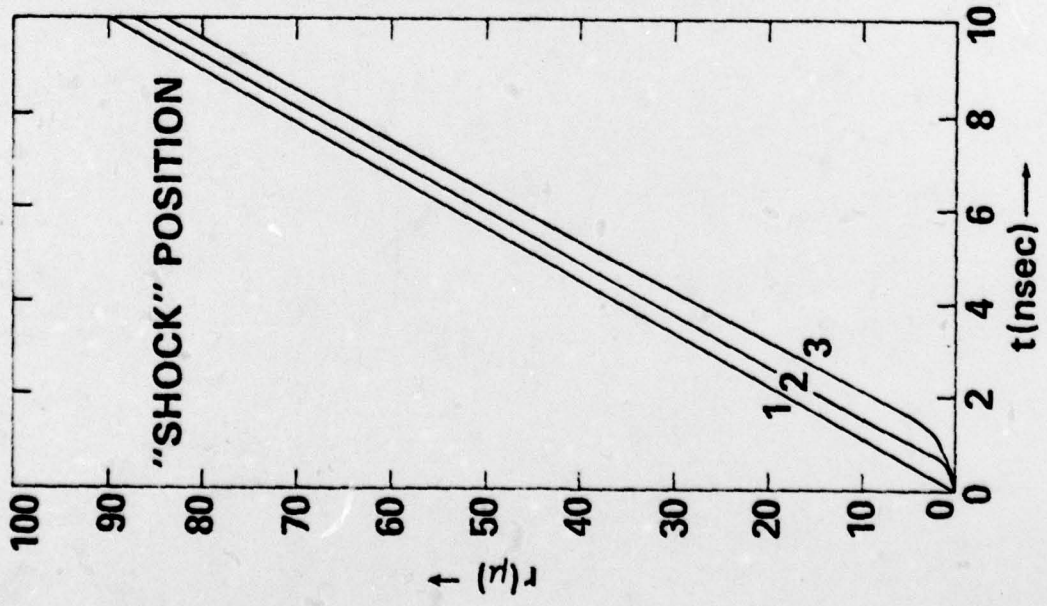


Figure 3

MODE AMPLITUDES (A)

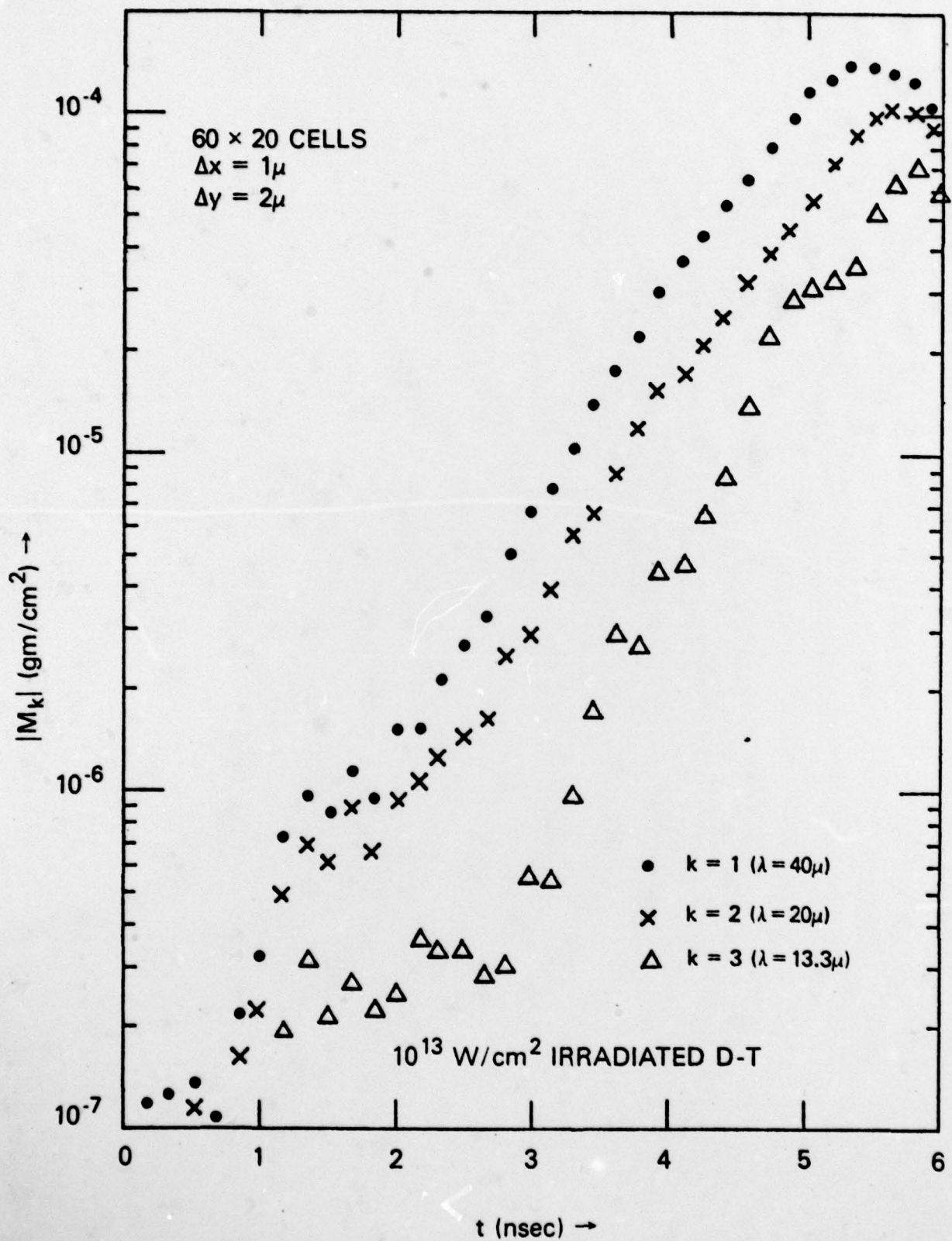


Figure 4

ABLATION LAYER RAYLEIGH-TAYLOR DISPERSION RELATION

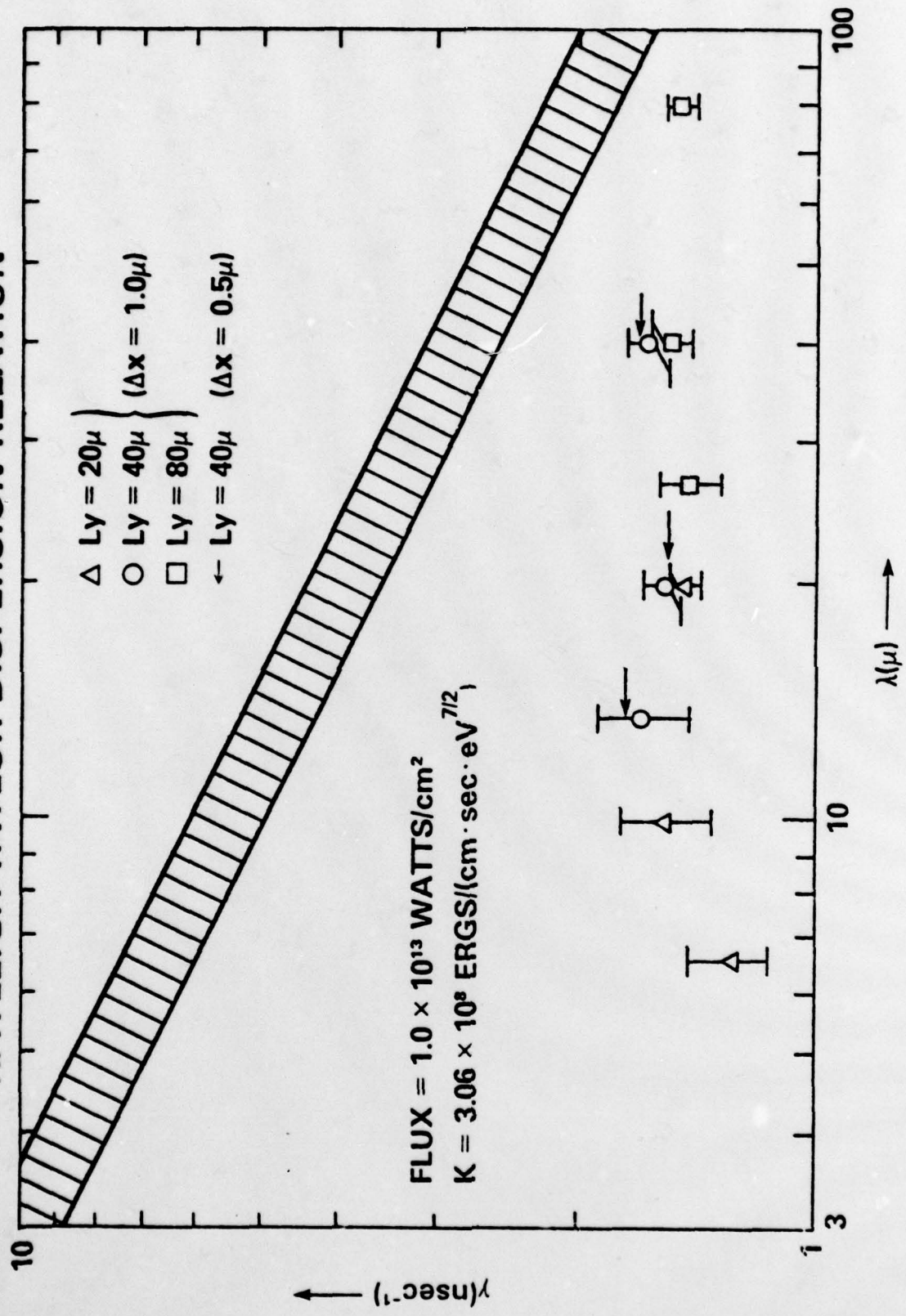


Figure 5

Jan 1978

ABLATION LAYER RAYLEIGH-TAYLOR INSTABILITY

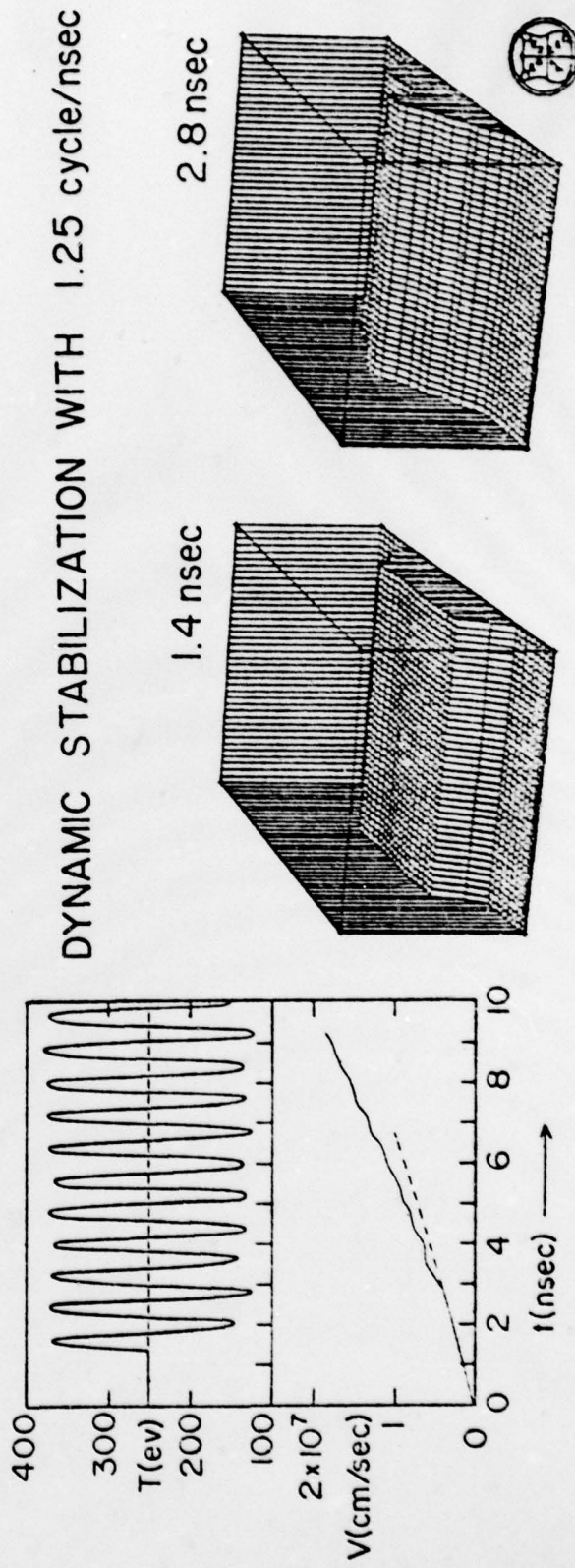
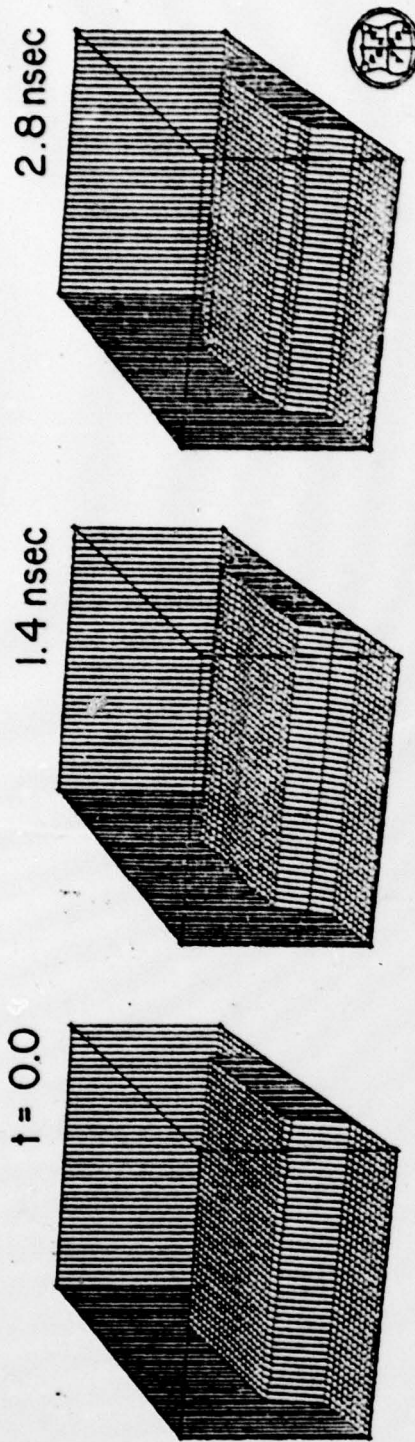
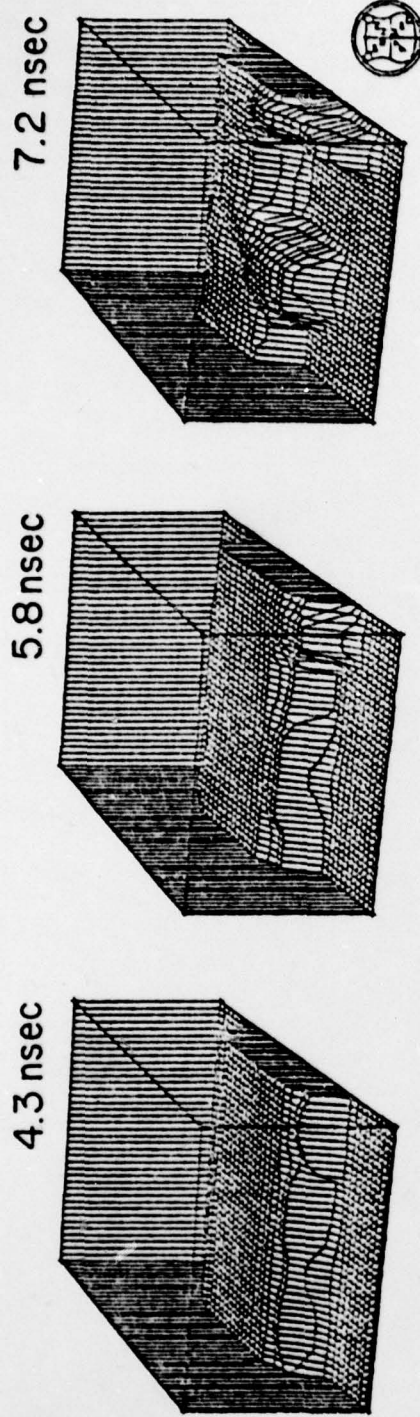


Figure 6

Jan 1978

ABLATION LAYER RAYLEIGH - TAYLOR INSTABILITY



DYNAMIC STABILIZATION WITH 1.25 cycle/nsec

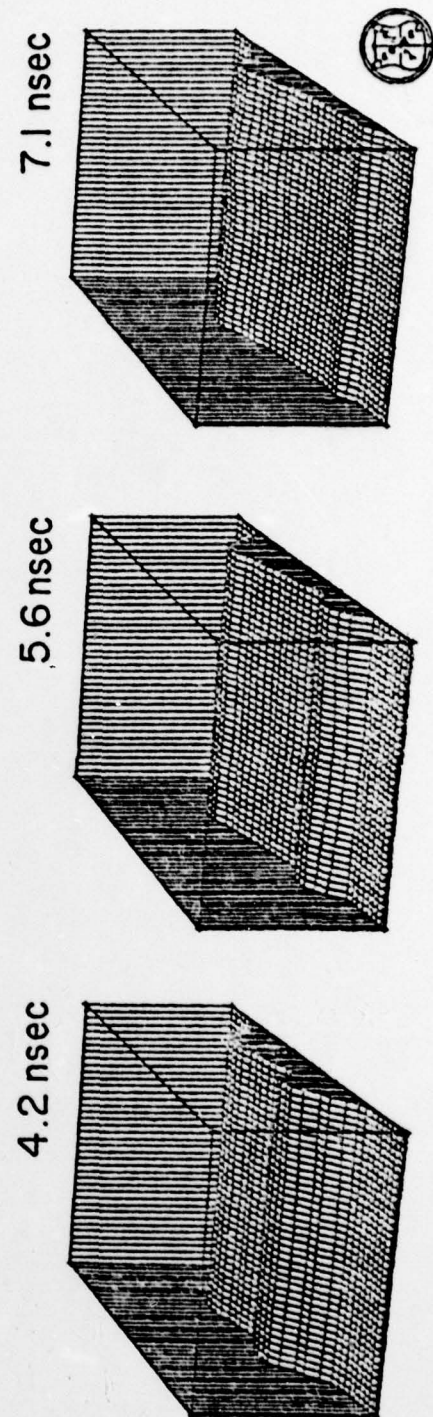
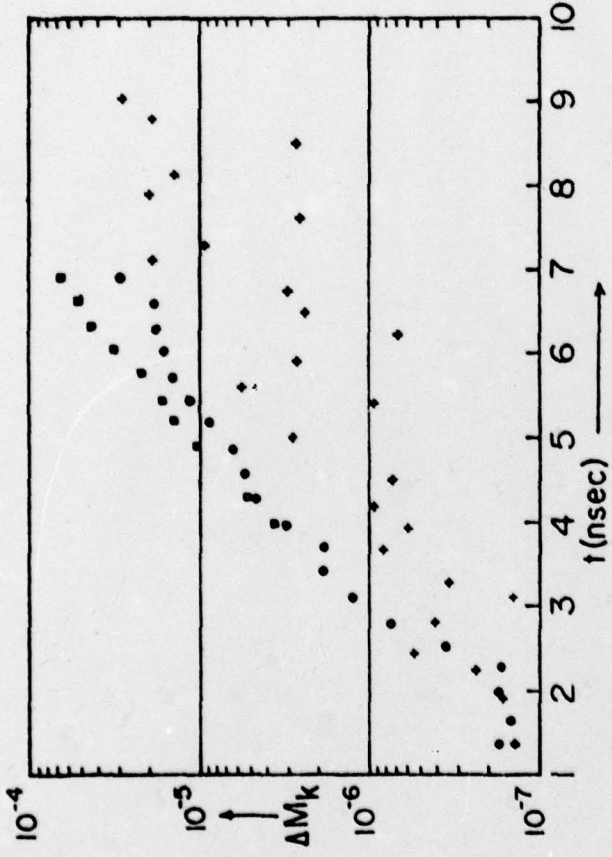


Figure 6 (continued)

Jan 1978



DYNAMIC STABILIZATION WITH 1.25 cycle/nsec

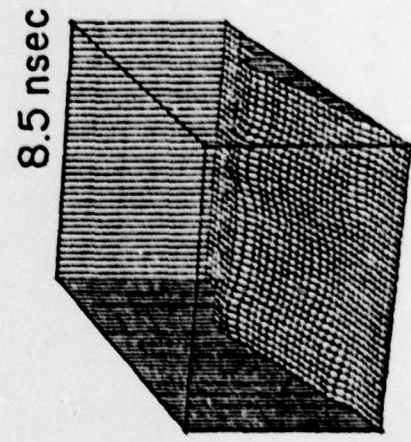
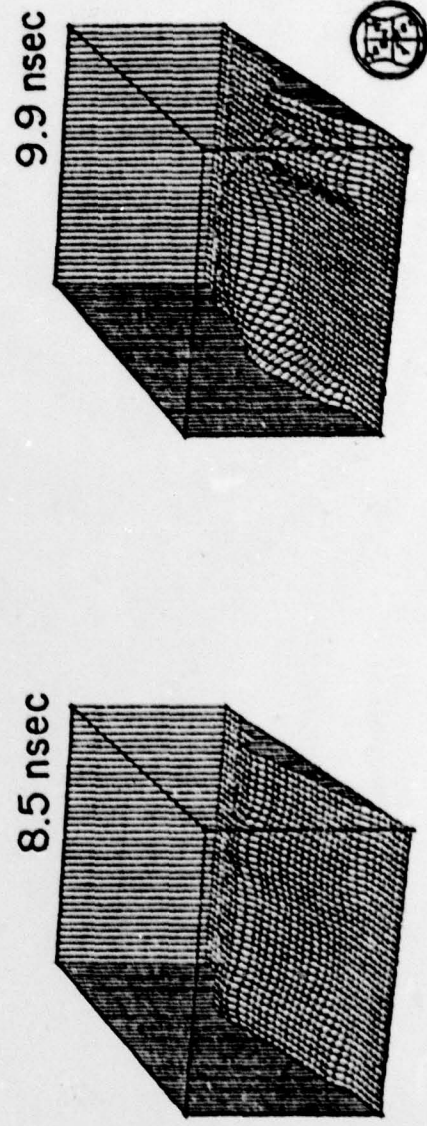


Figure 6 (continued)

RAYLEIGH-TAYLOR INSTABILITIES
GENERATED BY A SUPPORT WEB

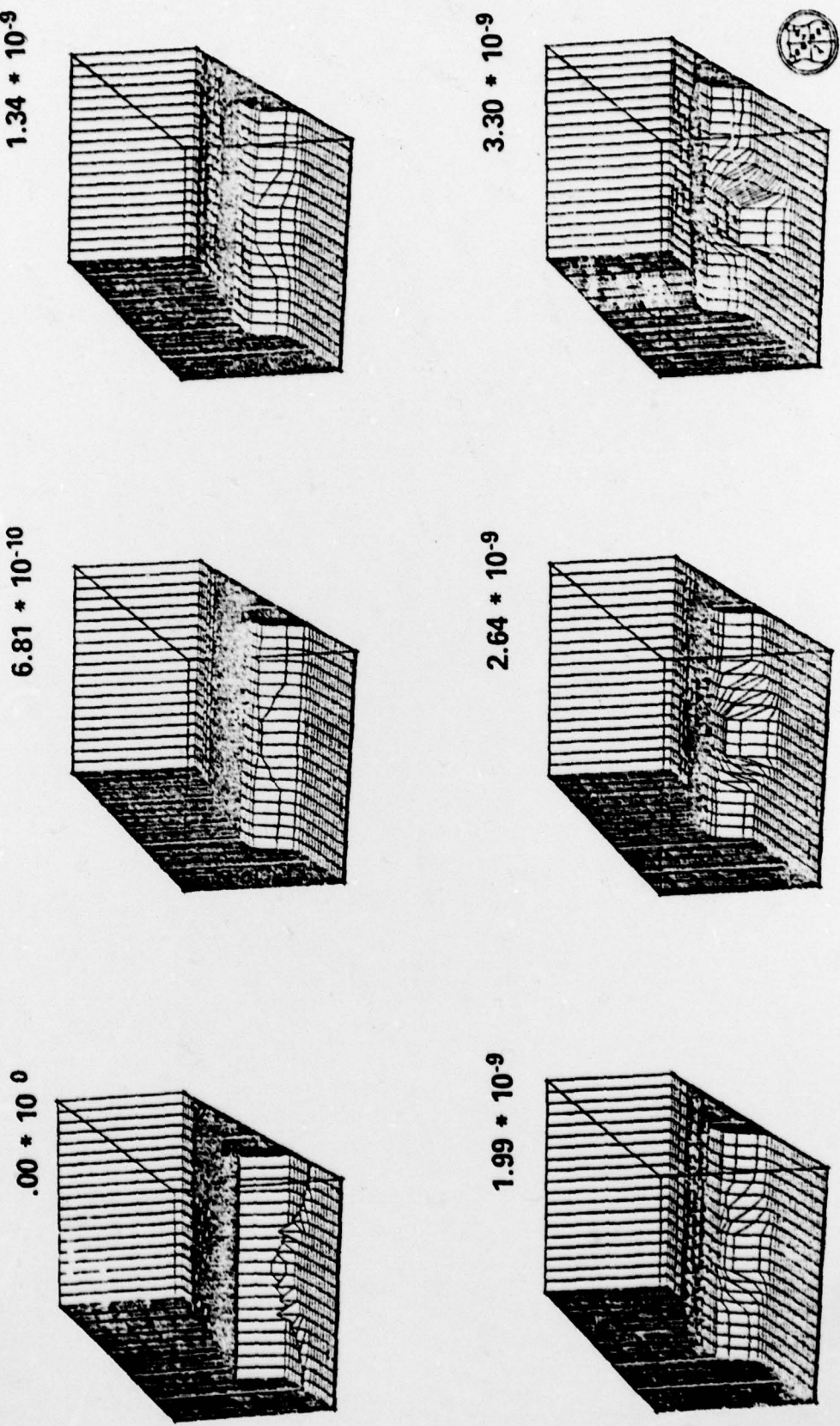
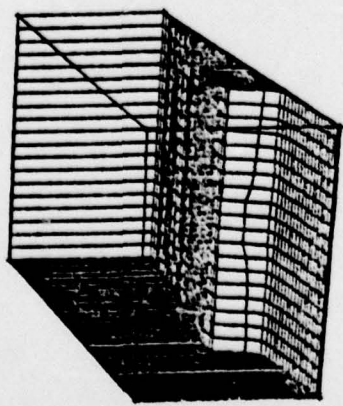


Figure 7

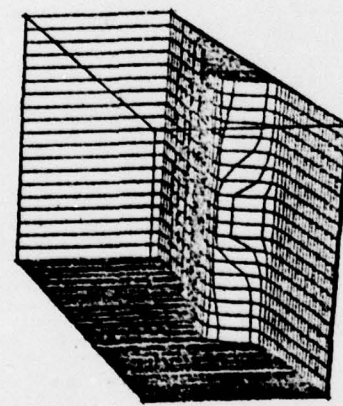
SUPPORT WEB (CONT.)

REDUCED WEB ($\rho_{MEM} = \rho_{MEM}/5$)

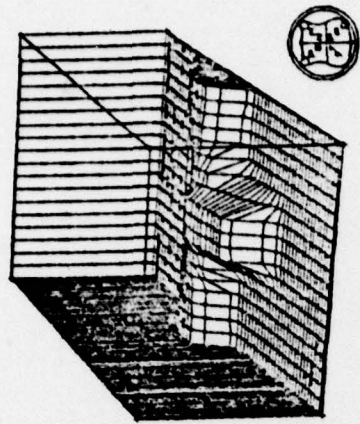
$1.34 * 10^{-9}$



$2.65 * 10^{-9}$

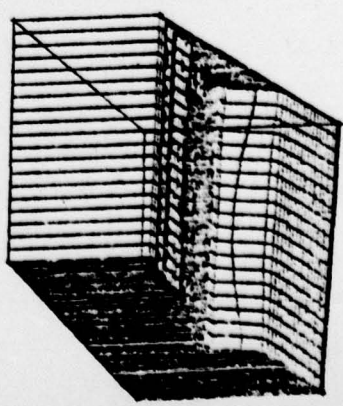


$3.91 * 10^{-9}$

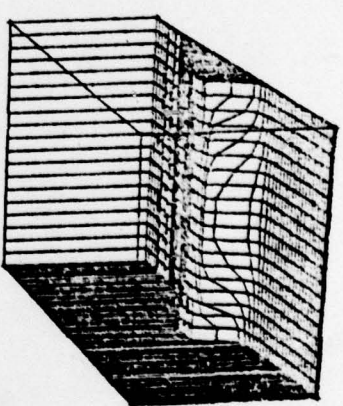


DISPLACED WEB ($\Delta x = 5\mu$)

$1.34 * 10^{-9}$



$2.64 * 10^{-9}$



$3.92 * 10^{-9}$

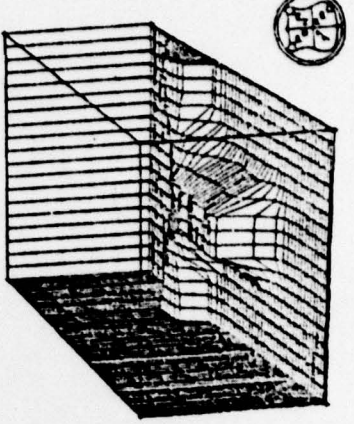


Figure 8

SUPPORT WEB MODE AMPLITUDES

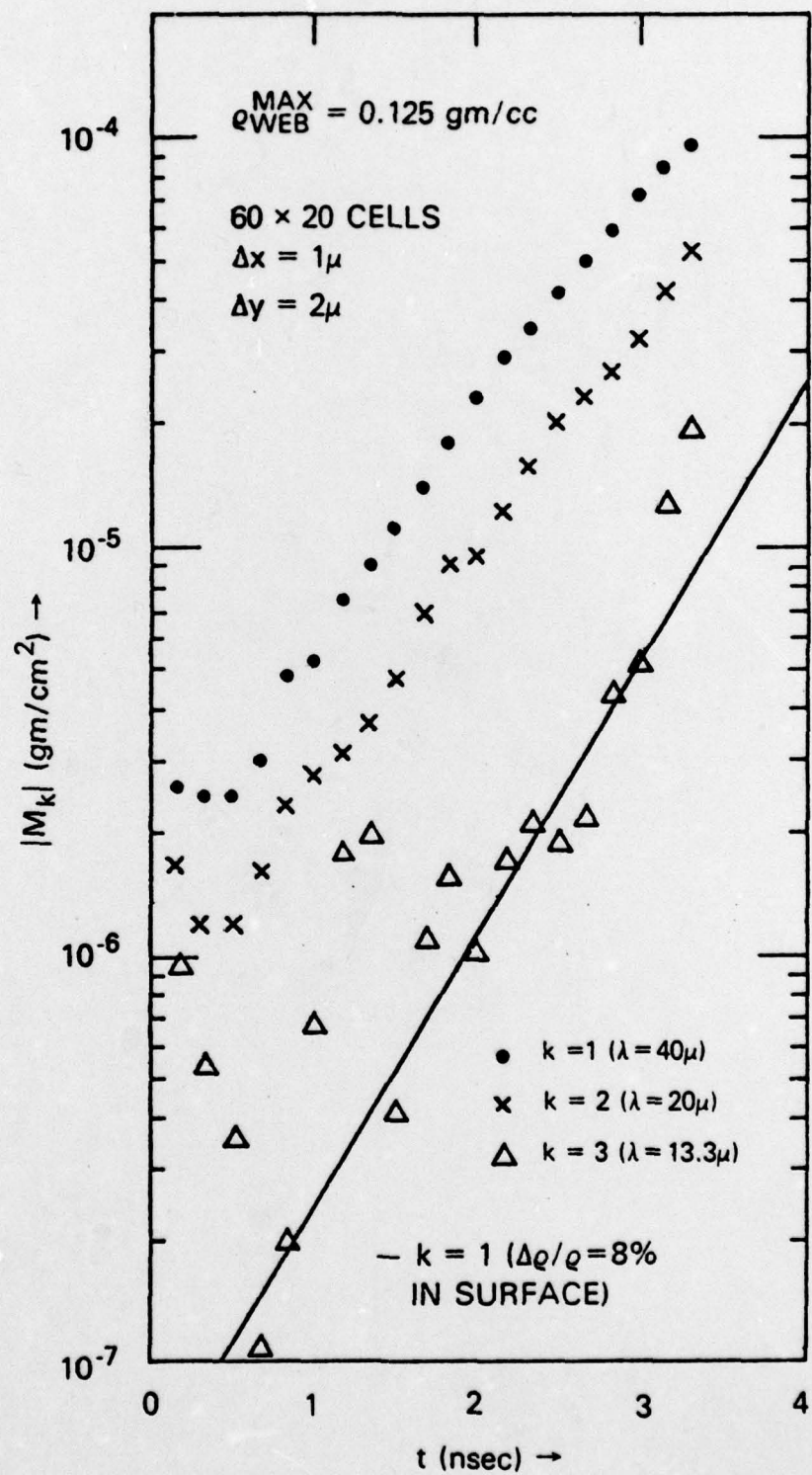


Figure 9

**5% VARIATION IN LASER INTENSITY
FOR 10^{13} w/cm² IRRADIATED D-T**

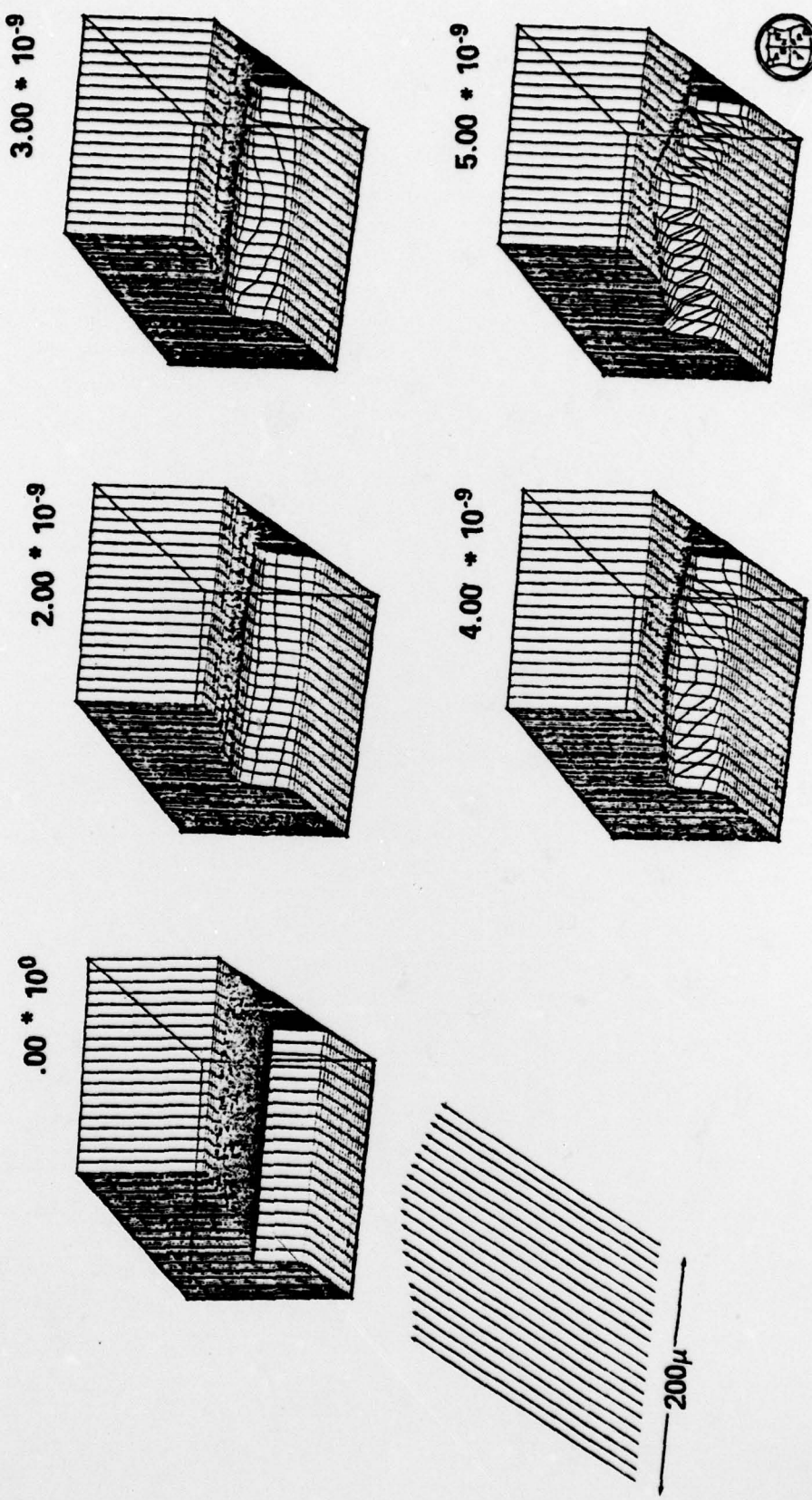


Figure 10

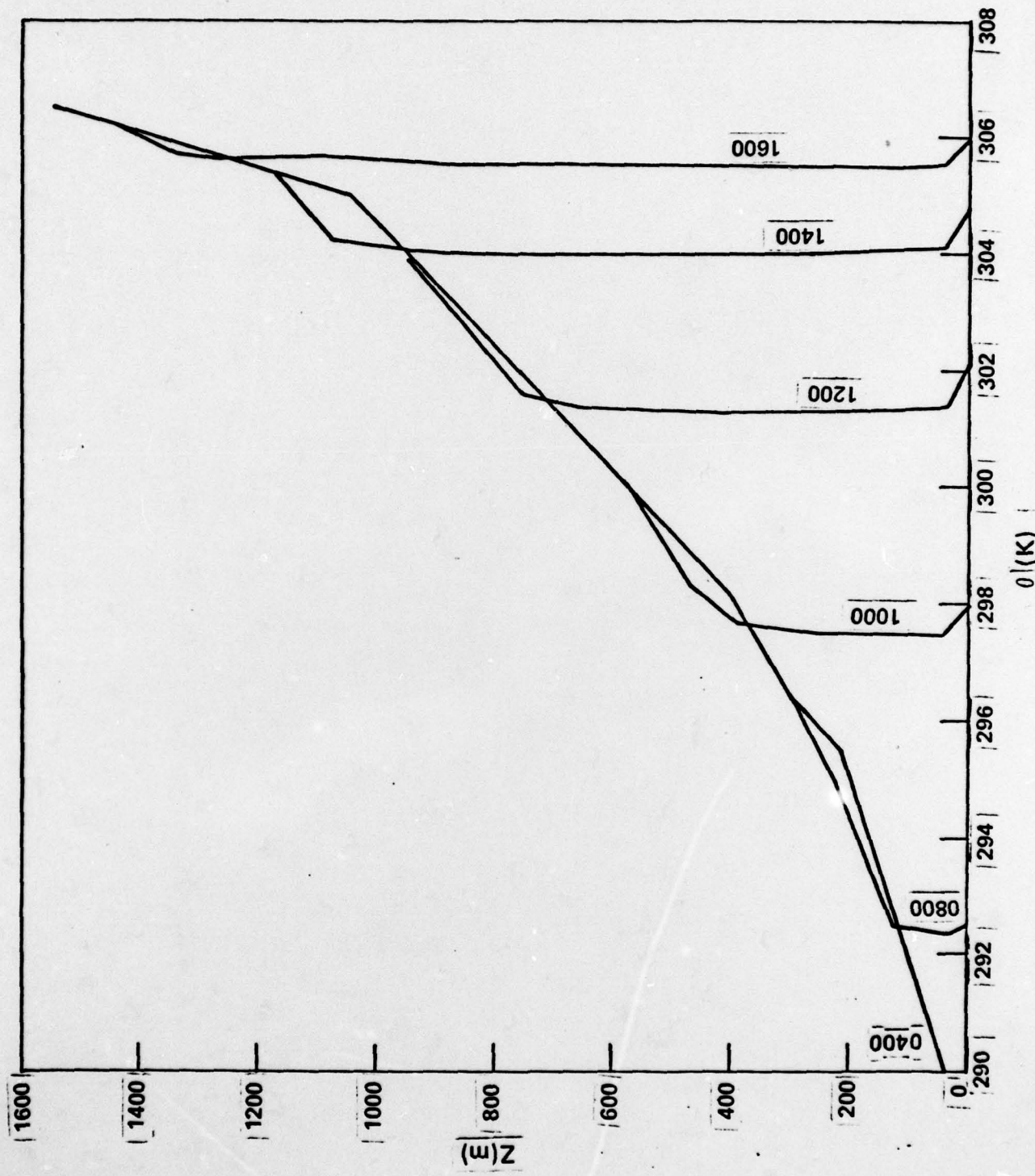


Figure 11

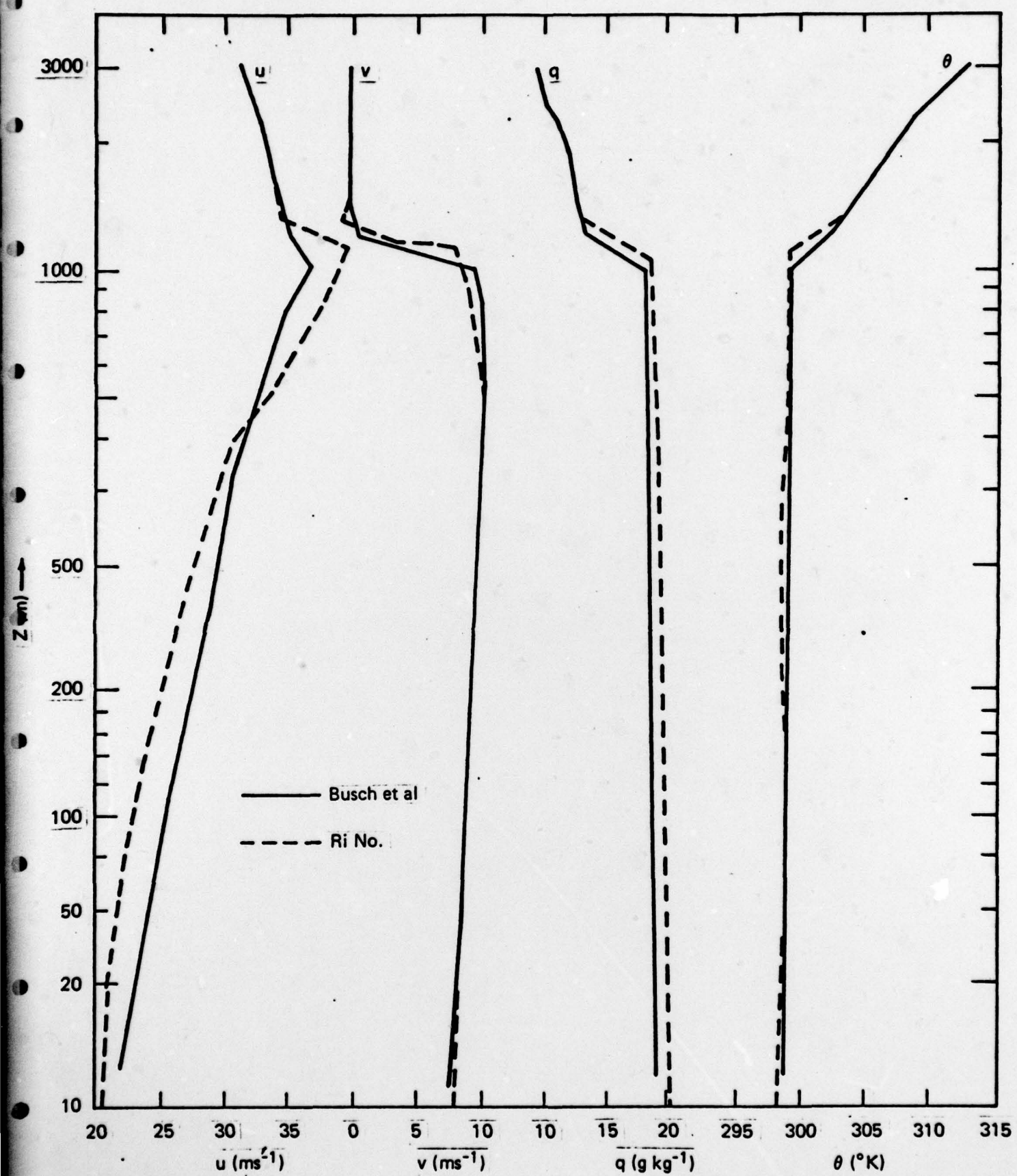


Figure 12

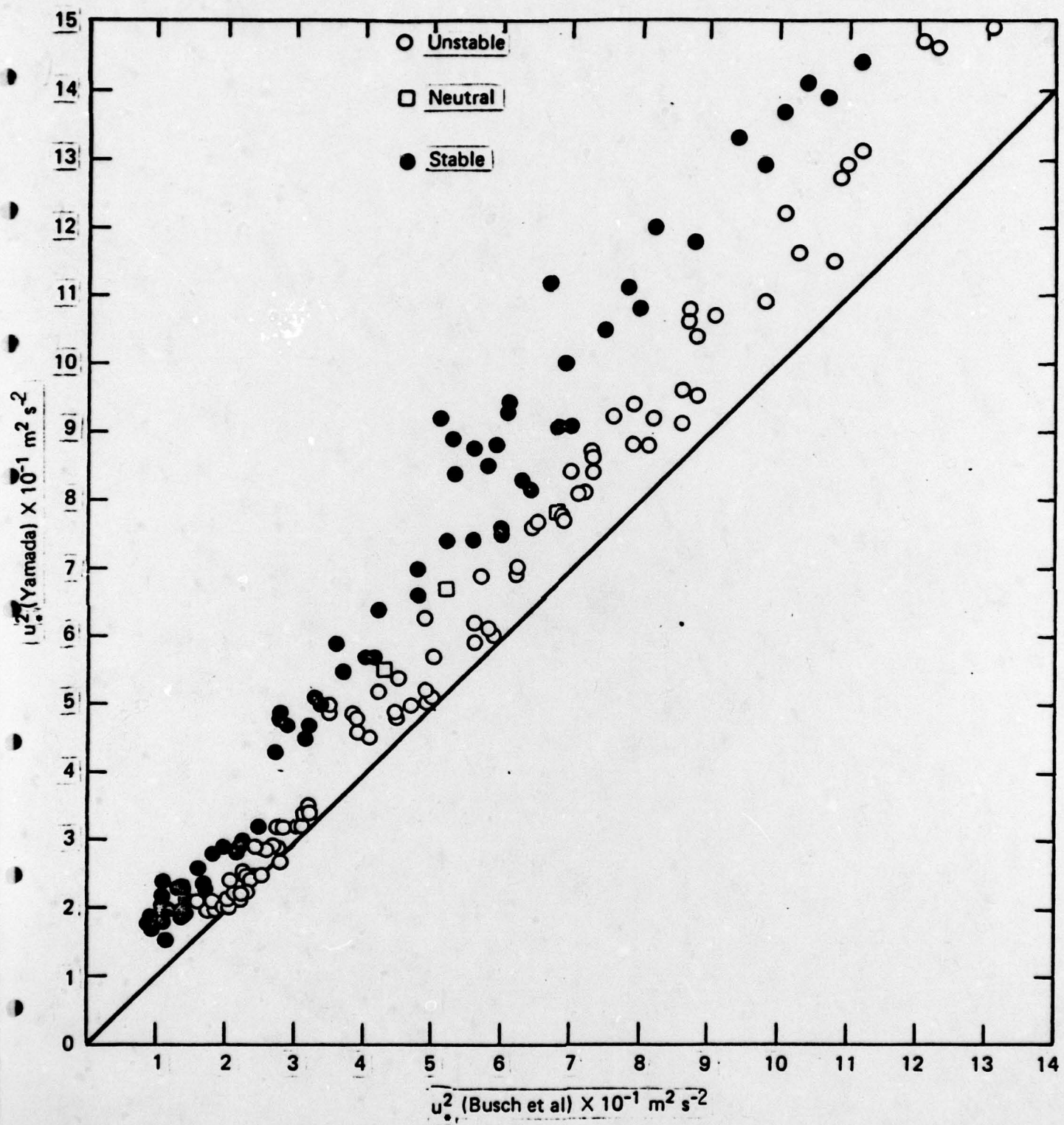


Figure 13

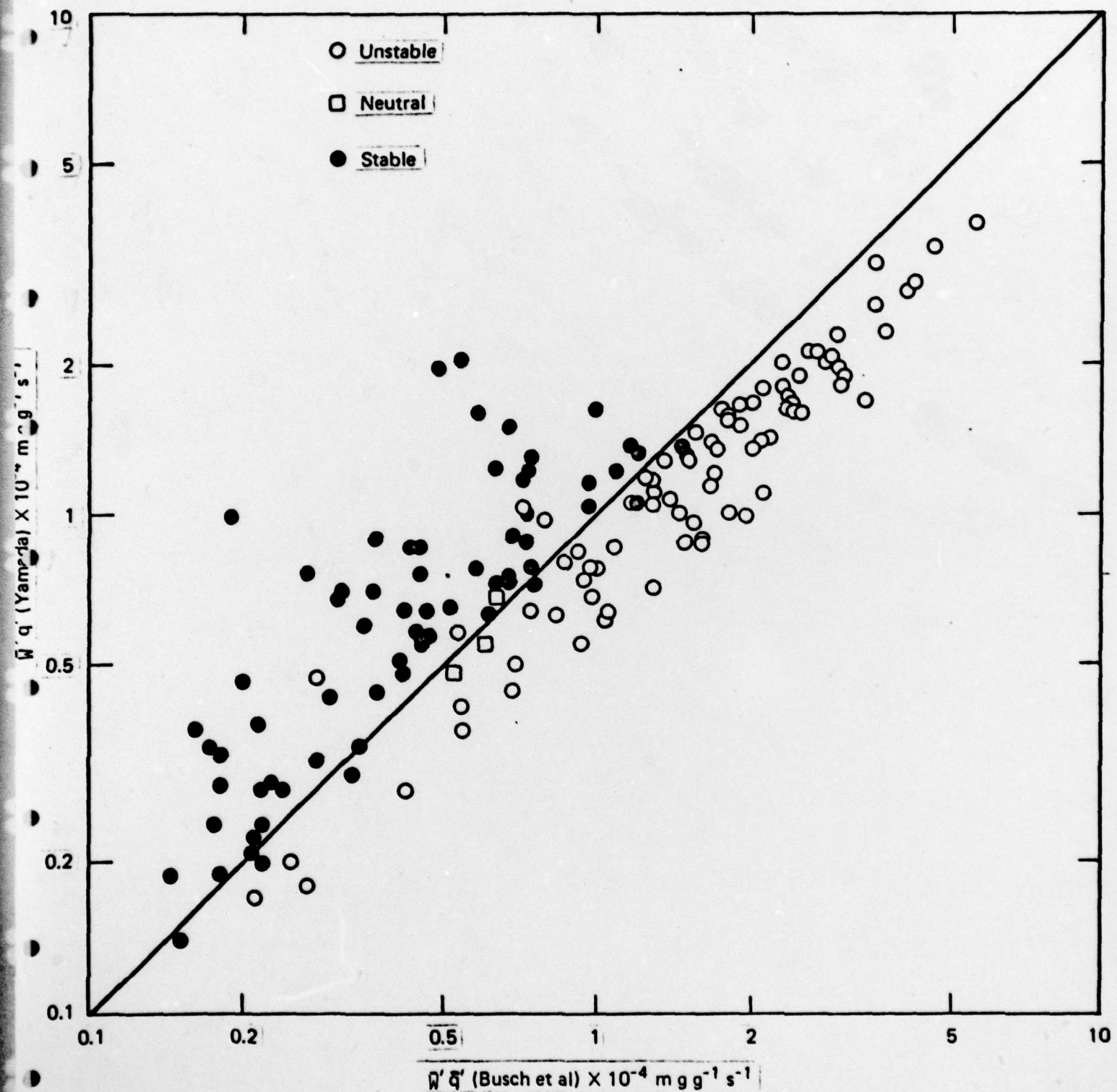


Figure 14